Article type: Full Paper

Title **((Porous silicon nanoneedles modulate endocytosis to deliver biological payloads))**

Author(s), and Corresponding Author(s)
Sahana Gopal[1,2], Ciro Chiappini[2,†]*, Jelle Penders[2], Vincent Leonardo[2], Hyejeong Seong[2]
Stephen Rothery[3], Yuri Korchev[1], Andrew Shevchuk[1]*, Molly M. Stevens[2,4,5]*

Dr. Sahana Gopal, Dr. Andrew Shevchuk, Prof. Yuri Korchev
[1]Department of Medicine, Imperial College London,
Hammersmith Hospital, Du Cane Road,
London W12 0NN, United Kingdom
E-mail: a.shevchuk@imperial.ac.uk

Dr. Sahana Gopal, Dr. Ciro Chiappini, Jelle Penders, Vincent Leonardo, Dr. Hyejeong Seong, Prof. Molly M. Stevens
[2]Department of Materials, [4]Department of Bioengineering, [5]Institute of Biomedical Engineering, Imperial College London,
Royal School of Mines, Prince Consort Road,
London SW7 2AZ, United Kingdom
E-mail: m.stevens@imperial.ac.uk
E-mail: ciro.chiappini@kcl.ac.uk

Mr. Stephen Rothery
[3]Facility for Light Microscopy, Imperial College London,
Sir Alexander Fleming Building, Exhibition Road,
London SW7 2BB, United Kingdom

Dr. Ciro Chiappini
[†]Current address
Department of Craniofacial Development and Stem Cell Biology, Kings College London
Floor 27, Guy's Hospital,
SE1 9RT
London, United Kingdom

Keywords: Biointerface, nanoneedles, porous silicon, drug delivery, endocytosis

Owing to their ability to efficiently deliver biological cargo and sense the intracellular milieu, vertical arrays of high aspect ratio nanostructures, known as nanoneedles, are being developed as minimally invasive tools for cell manipulation. However, little is known of the mechanisms of cargo transfer across the cell membrane-nanoneedle interface. Particularly, the contributions of membrane piercing, modulation of membrane permeability and endocytosis to cargo transfer remain largely unexplored. Here, combining state-of-the-art electron and scanning ion

1

conductance microscopy with molecular biology techniques, we show that porous silicon nanoneedle arrays concurrently stimulate independent endocytic pathways which contribute to enhanced biomolecule delivery into human mesenchymal stem cells. Electron microscopy of the cell membrane at nanoneedle sites shows an intact lipid bilayer, accompanied by an accumulation of clathrin-coated pits and caveolae. Nanoneedles enhance the internalisation of biomolecular markers of endocytosis, highlighting the concurrent activation of caveolae- and clathrin-mediated endocytosis, alongside macropinocytosis. These events contribute to the nanoneedle-mediated delivery (nanoinjection) of nucleic acids into human stem cells, which distribute across the cytosol and the endolysosomal system. This data extends the understanding of how nanoneedles modulate biological processes to mediate interaction with the intracellular space, providing indications for the rational design of improved cell-manipulation technologies.

1. Introduction

Gaining access to the intracellular space with minimal toxicity is a key feature in developing efficient strategies for drug delivery[1] and intracellular sensing.[2] Vertical high-aspect ratio nanoneedles,[3–9] have demonstrated a broad versatility to efficiently sense[2] and deliver[10] to the cell interior. Successful delivery of exogenous materials in the form of nucleic acids,[4,5,9] proteins,[5] metabolites[11] and cell-impermeable[12] nanoparticles by nanoneedle arrays, has now been independently demonstrated for a broad range of geometries, material compositions and cell types. Moreover, the intimate interface established with the cell membrane has enabled nanoneedles to sense proteins,[13] metabolites[14] and lipids[15] in the intracellular milieu as well as to stimulate and record action potentials of large arrays of individual excitable cells.[7,16,17] Nanoneedle arrays promise to be a safe and effective platform for nucleic acid delivery that compares favourably with microinjection and electroporation, thanks to its ease of use, high throughput, elevated biocompatibility and efficient delivery.

Despite rapid advances that culminated with their first use for *in-situ* gene therapy,[9] there is a need to improve the understanding of nanoneedle-mediated delivery in order to rationally design platforms for efficient clinical translation. Biomolecules delivered from nanoneedles display biological activity, highlighting an underlying mechanism that traffics them to their target site of action either in the cytosol (siRNA,[9] proteins[5] or peptides[13]) or in the nucleus (plasmid DNA[9]). This evidence of efficient delivery led to the initial assumption that nanoneedles traversed the cell membrane to directly deliver biomolecules into the cytoplasm. Pioneering studies with atomic force microscopy (AFM) operated nanoneedles supported this assumption, showing systematic drops in the force-displacement curve during interaction with synthetic lipid bilayers[18,19] and membranes of cells in culture,[20–23] attributed to breaching of the cell membrane. The local quenching of Green Fluorescent Protein (GFP) fluorescence upon nanoneedle delivery of membrane-impermeant Co^{2+} ions supported this view[24].

Yet, direct evidence from microscopy analysis of the cell-nanoneedle interface, invariably showed an intact cell membrane around the nanostructures. Transmission electron microscopy (TEM) analysis of cells on lower aspect nanoneedles displayed a continuous cell membrane wrapping around all the pillars observed.[25] Similarly, studies of nanoneedles of different geometries and surface chemistries showed that at least 95% of the nanoneedles were enclosed within a membrane, with a determination not possible only in the case of four amino-silane coated nanoneedles.[26] In agreement with this data, a more recent microscopy study showed cell membrane wrapping around nanoneedles of a range of lateral dimensions between 80 nm and 1 µm.[27] Further, all recent attempts using nanoneedles to sense intracellular potentials in excitable cells, agree on the need for an initial electroporation or optoporation in order to gain access to the cytosol, and that such access is only temporary, albeit much longer than conventional clamping methods.[7,16,28,27] Raman spectroscopy also allowed identifying the initial presence of a membrane wrapping around SERS active hollow nanoneedles, its disruption upon poration and the ensuing resealing process, that led to changes in membrane

composition.[15] Overall these findings indicate that a simple membrane penetration model does not fully describe the uniqueness and complexity of the cell-nanoneedle interface, calling for more in-depth investigations of its nature, and of the mechanisms that enable intracellular delivery.

For instance, we must consider the crucial role played by endocytosis in trafficking cargo from the cell membrane, a dynamic and complex system that is highly responsive to external signals, both mechanical and biochemical. Indeed, deforming the cell membrane, as nanoneedles do, can modulate the local composition of lipids and proteins,[29] inducing the accumulation of intracellular scaffolding structures that initiate clathrin or caveolae-mediated endocytosis.[30] High-aspect nanostructures that locally deform the membrane can accumulate scaffolding proteins and endocytic pits.[31–33] However, the contribution of endocytosis to biomolecule delivery from nanoneedles, and its role on determining the fate of the payload still needs to be clarified.

In this study, we investigate the interface between the cell membrane and recently developed porous silicon nanoneedles[9,12] in relation to their capacity to deliver biological payloads in human mesenchymal stem cells. In particular, we assess the ability of porous silicon nanoneedles to deliver biological cargo via endocytosis, while negotiating the cell membrane. Using a variety of state-of-the-art microscopy techniques, we present a study of plasma membrane remodelling on nanoneedles that contributes to intracellular entry. Moreover, we study the fate of the delivered endocytosis-specific cargo within the cytoplasm, highlighting the significant role of endocytic pathways in nanoneedle-mediated delivery (nanoinjection). Finally, the significant endolysosomal trafficking of nanoneedle-injected siRNA highlights a role for endocytosis in nucleic acid uptake, while concurrently validating its cytosolic delivery and biological activity by gene silencing. These results provide fundamental insight into the contribution of topographic stimuli on intracellular delivery in non-endocytic cells, which has

implications for the design of next generation stem cell manipulation strategies involving intracellular biomolecule delivery and interrogation.

2. Results and Discussion

2.1. Membrane response upon nanoneedle interfacing

In order to assess the membrane response to interfacing with porous silicon nanoneedles, the apical membrane morphology of human mesenchymal stem cells (hMSCs) was visualized on nanoneedle arrays and flat silicon substrates using a combination of electron and scanning ion conductance microscopy (SICM) techniques. SICM enabled label-free, non-invasive mapping of the topography of the apical cell membrane in its native state[34–36] (Figure S1a, Supporting Information). After 6 hours of culture, the apical surface of hMSCs on nanoneedles showed numerous protrusions in random orientations akin to dorsal membrane ruffles seen in cells actively participating in macropinocytosis[37] and remodelling their actin cytoskeleton[38] (Figure 1a, Figure S1b, S1c, Supporting Information). It is in these regions that actin-related protein 2/3 (ARP2/3) complexes and vesicle scission proteins such as dynamins are known to localize.[39] Membrane ruffling led to a 1.8-2-fold increase in surface roughness (R_{rms} and R_a) of the apical membrane of cells interfaced with nanoneedles compared to those cultured on flat silicon wafers (FSW) (Figure 1b, 1c). To characterize the morphology of the basal membrane in contact with the nanoneedles, we used a recently developed focused ion beam scanning electron microscopy (FIB-SEM) approach[9,40] for *in-situ* slice-and-view[40,41] (Figure 1d, Figure S2 a-e, Supporting Information), alongside analysis of resin-embedded sections by TEM (Figure 1e, Figure S3, Supporting Information). FIB-SEM showed the basal membrane of hMSCs wrapping around individual nanoneedles without discontinuities evident at 20 nm resolution (Figure S2d, S2e, Supporting Information). Higher resolution TEM micrographs of FIB-milled sections showed extreme vicinity (in the order of nanometers) between the nanoneedles and the membrane at the interface and confirmed membrane continuity at 4 nm resolution (Figure 1e).

5

2.2 Triggering endocytosis at sites of nanoneedle interfacing

In the absence of visible membrane penetration or discontinuities for long-term interfacing, and given the observed membrane ruffling, endocytosis represents a viable mechanism that can contribute to payload delivery. Immunofluorescence analysis highlighted the localization of caveolin-1 (CAV-1, Figure 2a-d), a key protein involved in caveolae-mediated endocytosis (CavME) and clathrin light chain (CLC, Figure 2e-h), a clathrin coat protein for clathrin-mediated endocytosis (CME) after 6 hours of interfacing. Both CAV-1 and CLC co-localized with nanoneedles at the basal membrane, as they clustered with periodic intensity. Fourier transform analysis confirmed that the period (1.967 +/- 0.05 μm) matched the nanoneedle spacing (2 μm) (Figure 2d, 2h). The same proteins at the apical membrane were unaffected by the nanoneedles and we observed no periodicity basally or apically for hMSCs on FSW (Figure 2c, 2g). Moreover, the total protein expression levels of CAV-1 and CLC did not increase on nanoneedles suggesting that this response is local to the membrane-nanoneedle interface (Figure S4, Supporting Information). Indeed, FIB-SEM analysis confirmed the assembly of these endocytic proteins into spherical coated pits and flask shaped invaginations in the size range of clathrin coated pits (CCP) and caveolae (Figure 2i, Figure S2e, Supporting Information), and their preferential accumulation near the tips and sides of the nanoneedles (Figure 2j, 2k). Previous reports of cells cultured on nanopillars suggest that caveolae are not sensitive to membrane curvature.[31] However electron microscopy, confocal imaging and delivery of caveolae-specific cargo in our system indicate that caveolae are key players during interfacing, most likely through their ability to sense membrane tension rather than curvature in a mechanically stressed environment.[42] These data indicate that nanoneedles induce local membrane deformation that accumulates functional endocytic vesicles.

2.3 Pathway-specific endocytosis accounts for cytosolic delivery

Given the accumulation of endocytic vesicles at the nanoneedle interface and the membrane ruffling, we investigated whether and to what extent nanoneedles stimulated specific endocytic pathways. We assessed CME by Transferrin (Tfn) uptake, CavME by internalization of Cholera toxin B-subunit (CTxB) and macropinocytosis (MP) by uptake of Dextran (Dex) chains in the size range of 10 kDa to 70 kDa (Figure 3a, clockwise). We measured the adsorption efficiency of Tfn, CTxB and Dex to find that these cargoes adsorbed in similar amounts on nanoneedles and FSW suggesting that the maximal loading of the nanoneedle substrate is dependent on the size and charge of the cargo, nanoneedle pore size and surface charge rather than total surface area (Figure S5, Supporting Information). After 24 hours, Tfn, CTxB and Dex 10, 40 and 70 kDa were all internalized more efficiently by cells cultured on nanoneedle arrays compared to FSW as indicated by the significant increase in the percentage of positive cells for each of the cargo (Figure 3a, Figure S7-S11, Supporting Information).

In order to assess the proportion of endocytic cargo that enters the endolysomal system during nanoneedle-mediated delivery, we assessed biomolecules known to internalize through specific endocytic pathways for their co-localization with early endosomes and lysosomes. In addition, we determined the co-localization of Tfn (known to enter by CME) against CLC, and the co-localization of CTxB (known to enter by CavME) with Cav-1 at 24 hours. At this point the nanoneedles have degraded[9] and no array-like pattern of Cav-1 and CLC was observed. Tfn co-localized with CLC (46 ± 16%) and LAMP1 (49 ± 20%) and Early Endosome Antigen 1 (EEA1, 33 ± 12%), indicating that Tfn may be recycled to the cell surface (associated with CLC at cell surface) and trafficked into lysosomes (Figure 3b). The extent of co-localization for CME and CavME cargoes with endolysosomal compartments and carrier proteins was highly variable. For instance, the co-localization of CTxB with its carrier Cav-1 and with EEA1 ranged from below 20% in some cases to above 90% in others (Figure 3c, graph panel). This variation suggests that nanoneedles enable sustained delivery of CTxB resulting in cargo at different stages of trafficking along each pathway. CTxB however co-localized highly with LAMP1,

7

suggesting that CavME stimulated by nanoneedles accumulated within lysosomes. Unsurprisingly, Dex showed highly consistent degrees of co-localization with endosomes and lysosomes (20-30%), possibly owing to the fact that macropinocytosis occurs from the apical cell surface and relies on release of fluid phase markers into the surrounding media for internalization rather than from the basal cell surface in contact with the nanoneedles (Figure 3d). Lastly, we assessed the fate of each of these cargoes within the endolysosomal system by combining their co-localization with respective carriers, endosomes and lysosomes to find that CTxB was trafficked into the endolysosomal system to the greatest extent ($65 \pm 20\%$), followed by Tfn ($45 \pm 17\%$), and Dex ($38 \pm 11\%$) (Figure 3e). This indicates that specific endocytic pathways are activated by nanoneedles, and account for a significant fraction, but not the entirety, of the total delivery of cargo-specific payload.

2.4 Nucleic acid fate following nanoneedle delivery

If endocytosis is the key mechanism of internalization by nanoinjection, the entrapment of biofunctional payloads within the endolysosomal system could hamper their functionality. To test this hypothesis we investigated the trafficking of nanoinjected siRNA targeting GAPDH and probed its biological activity, which relies on the colocalization of non-degraded siRNA with the RNA-induced silencing complex (RISC) in the cytosol.[43] Indeed, nanoinjection significantly improved intracellular delivery of siRNA-GAPDH (Figure 4a). After 24 hours of interfacing, the siRNA localized in the cytoplasm of hMSCs with a considerable amount of punctate signal, typically in the perinuclear region (Figure 4b). siRNA could be seen co-localizing with Cav-1, CLC, EEA1 and LAMP1 to different extents (Figure 4c – f), and its co-localization with these components was quantified. An average of $45 \pm 13\%$ of siRNAs co-localized with Cav-1, $34 \pm 9\%$ of siRNAs co-localized with CLC, $44 \pm 14\%$ of siRNA with EEA1 and $40 \pm 13\%$ of the siRNAs were entrapped within LAMP1 positive lysosomes, indicating that a substantial percentage of nucleic acids enter the endolysosomal pathway (Figure 4g). By considering the co-localization of siRNA with the combined signal of EEA1,

Lamp1, CLC and Cav-1, $62 \pm 16\%$ of siRNA was trafficked into the endolysosomal pathway (Figure 4g). Nevertheless, nanoinjection of siRNA-GAPDH induced a statistically significant $43 \pm 14\%$ reduction in GAPDH expression in hMSCs compared to control in each experiment (N = 3, *p < 0.05, Student's paired t-test, Table S1, Supporting Information), indicating that a proportion of the remaining 38% of nanoinjected siRNAs are trafficked outside of endolysosomal pathway and can mediate biological functions in the cytosol.

3. Conclusion

Overall, our results demonstrate that nanoneedles improve the internalisation of pathway-specific payloads and nucleic acids. This delivery is at least partly mediated by endocytic processes which are upregulated selectively at the cell-nanoneedle interface, leading to the endolysosomal localization of large proportions of the payloads. Nonetheless, a significant fraction of each payload (38% for siRNA) is trafficked alternatively and retains biological function in the cytosol. The active cytosolic fraction of payload could result from endosomal escape or concurrent delivery mechanisms that bypass the endolysosomal system. In the literature, studies of nanoneedle-mediated gene therapy have shown transfection efficiencies widely varying between 0% and >90% depending on nanoneedle properties and cell type.[3–5,9,44] The engagement of specific endocytic pathways can regulate payload fate and could play a significant role in the broad differences observed. This study highlights that these aspects should be investigated when developing nanoinjection strategies in order to optimize their efficiency.

4. Experimental Section (Available in Supplementary)

Supporting Information

References

[1] M. P. Stewart, A. Sharei, X. Ding, G. Sahay, R. Langer, K. F. Jensen, *Nature* **2016**, *538*, 183.

[2] C. Chiappini, *ACS Sens.* **2017**, *2*, 1086.

[3] T. E. McKnight, A. V. Melechko, G. D. Griffin, M. A. Guillorn, V. I. Merkulov, F. Serna, D. K. Hensley, M. J. Doktycz, D. H. Lowndes, M. L. Simpson, *Nanotechnology* **2003**, *14*, 551.

[4] W. Kim, J. K. Ng, M. E. Kunitake, B. R. Conklin, P. Yang, *J. Am. Chem. Soc.* **2007**, *129*, 7228.

[5] A. K. Shalek, J. T. Robinson, E. S. Karp, J. S. Lee, D.-R. Ahn, M.-H. Yoon, A. Sutton, M. Jorgolli, R. S. Gertner, T. S. Gujral, G. MacBeath, E. G. Yang, H. Park, *Proc Natl Acad Sci U S A* **2010**, *107*, 1870.

[6] J. J. VanDersarl, A. M. Xu, N. A. Melosh, *Nano Lett.* **2012**, *12*, 3881.

[7] C. Xie, Z. Lin, L. Hanson, Y. Cui, B. Cui, *Nat Nano* **2012**, *7*, 185.

[8] L. Hanson, W. Zhao, H.-Y. Lou, Z. C. Lin, S. W. Lee, P. Chowdary, Y. Cui, B. Cui, *Nat Nano* **2015**, *10*, 554.

[9] C. Chiappini, E. De Rosa, J. O. Martinez, X. Liu, J. Steele, M. M. Stevens, E. Tasciotti, *Nat Mater* **2015**, *14*, 532.

[10] R. Elnathan, M. Kwiat, F. Patolsky, N. H. Voelcker, *Nano Today* **2014**, *9*, 172.

[11] A. M. Xu, D. S. Wang, P. Shieh, Y. Cao, N. A. Melosh, *ChemBioChem* **2017**, *18*, 623.

[12] C. Chiappini, J. O. Martinez, E. De Rosa, C. S. Almeida, E. Tasciotti, M. M. Stevens, *ACS Nano* **2015**, *9*, 5500.

[13] C. Chiappini, P. Campagnolo, C. S. Almeida, N. Abbassi-Ghadi, L. W. Chow, G. B. Hanna, M. M. Stevens, *Adv. Mater.* **2015**, *27*, 5147.

[14] S. Choi, H. Kim, S. Y. Kim, E. G. Yang, *Nanoscale* **2016**, *8*, 11380.

[15] R. La Rocca, G. C. Messina, M. Dipalo, V. Shalabaeva, F. De Angelis, *Small* **2015**, *11*, 4632.

[16] J. Abbott, T. Ye, L. Qin, M. Jorgolli, R. S. Gertner, D. Ham, H. Park, *Nature Nanotechnology* **2017**, *12*, 460.

[17] J. T. Robinson, M. Jorgolli, A. K. Shalek, M.-H. Yoon, R. S. Gertner, H. Park, *Nat Nano* **2012**, *7*, 180.

[18] B. D. Almquist, N. A. Melosh, *PNAS* **2010**, *107*, 5815.

[19] B. D. Almquist, N. A. Melosh, *Nano Lett.* **2011**, *11*, 2066.

[20] I. Obataya, C. Nakamura, Han, N. Nakamura, J. Miyake, *Nano Lett.* **2005**, *5*, 27.

[21] S. W. Han, C. Nakamura, I. Obataya, N. Nakamura, J. Miyake, *Biosensors and Bioelectronics* **2005**, *20*, 2120.

[22] S. Han, C. Nakamura, I. Obataya, N. Nakamura, J. Miyake, *Biochemical and Biophysical Research Communications* **2005**, *332*, 633.

[23] S.-W. Han, C. Nakamura, N. Kotobuki, I. Obataya, H. Ohgushi, T. Nagamune, J. Miyake, *Nanomedicine: Nanotechnology, Biology and Medicine* **2008**, *4*, 215.

[24] A. M. Xu, A. Aalipour, S. Leal-Ortiz, A. H. Mekhdjian, X. Xie, A. R. Dunn, C. C. Garner, N. A. Melosh, *Nat Commun* **2014**, *5*, 3613.

[25] L. Hanson, Z. C. Lin, C. Xie, Y. Cui, B. Cui, *Nano Lett.* **2012**, *12*, 5815.

[26] T. Berthing, S. Bonde, K. R. Rostgaard, M. H. Madsen, C. B. Sørensen, J. Nygård, K. L. Martinez, *Nanotechnology* **2012**, *23*, 415102.

[27] M. Dipalo, A. F. McGuire, H.-Y. Lou, V. Caprettini, G. Melle, G. Bruno, C. Lubrano, L. Matino, X. Li, F. D. Angelis, B. Cui, F. Santoro, *Nano Letters* **2018**, DOI 10.1021/acs.nanolett.8b03163.

[28] Z. C. Lin, A. F. McGuire, P. W. Burridge, E. Matsa, H.-Y. Lou, J. C. Wu, B. Cui, *Microsystems & Nanoengineering* **2017**, *3*, 16080.

[29] M. Simunovic, G. A. Voth, A. Callan-Jones, P. Bassereau, *Trends Cell Biol* **2015**, *25*, 780.

[30] I. K. Jarsch, F. Daste, J. L. Gallop, *J Cell Biol* **2016**, *214*, 375.

[31] W. Zhao, L. Hanson, H.-Y. Lou, M. Akamatsu, P. D. Chowdary, F. Santoro, J. R. Marks, A. Grassart, D. G. Drubin, Y. Cui, B. Cui, *Nat Nano* **2017**, *12*, 750.

[32] M. J. Dalby, C. C. Berry, M. O. Riehle, D. S. Sutherland, H. Agheli, A. S. G. Curtis, *Exp. Cell Res.* **2004**, *295*, 387.

[33] C. Moerke, P. Mueller, B. Nebe, *Biomaterials* **2016**, *76*, 102.

[34] Y. E. Korchev, C. L. Bashford, M. Milovanovic, I. Vodyanoy, M. J. Lab, *Biophys. J.* **1997**, *73*, 653.

[35] J. Gorelik, N. N. Ali, S. H. S. Abdul Kadir, M. Lab, P. Stojkovic, L. Armstrong, E. V. Sviderskaya, Y. A. Negulyaev, D. Klenerman, D. C. Bennett, M. Lako, S. E. Harding, M. Stojkovic, Y. E. Korchev, *Tissue Eng Part C Methods* **2008**, *14*, 311.

[36] P. Novak, C. Li, A. I. Shevchuk, R. Stepanyan, M. Caldwell, S. Hughes, T. G. Smart, J. Gorelik, V. P. Ostanin, M. J. Lab, G. W. J. Moss, G. I. Frolenkov, D. Klenerman, Y. E. Korchev, *Nat Meth* **2009**, *6*, 279.

[37] M. C. Kerr, R. D. Teasdale, *Traffic* **2009**, *10*, 364.

[38] T. Itoh, J. Hasegawa, *J Biochem* **2013**, *153*, 21.

[39] J. D. Orth, E. W. Krueger, H. Cao, M. A. McNiven, *PNAS* **2002**, *99*, 167.

[40] F. Santoro, W. Zhao, L.-M. Joubert, L. Duan, J. Schnitker, Y. van de Burgt, H.-Y. Lou, B. Liu, A. Salleo, L. Cui, Y. Cui, B. Cui, *ACS Nano* **2017**, *11*, 8320.

[41] T. C. von Erlach, S. Bertazzo, M. A. Wozniak, C.-M. Horejs, S. A. Maynard, S. Attwood, B. K. Robinson, H. Autefage, C. Kallepitis, A. del R. Hernández, C. S. Chen, S. Goldoni, M. M. Stevens, *Nature Materials* **2018**, *17*, 237.

[42] B. Sinha, D. Köster, R. Ruez, P. Gonnord, M. Bastiani, D. Abankwa, R. V. Stan, G. Butler-Browne, B. Vedie, L. Johannes, N. Morone, R. G. Parton, G. Raposo, P. Sens, C. Lamaze, P. Nassoy, *Cell* **2011**, *144*, 402.

[43] A. J. Pratt, I. J. MacRae, *J Biol Chem* **2009**, *284*, 17897.

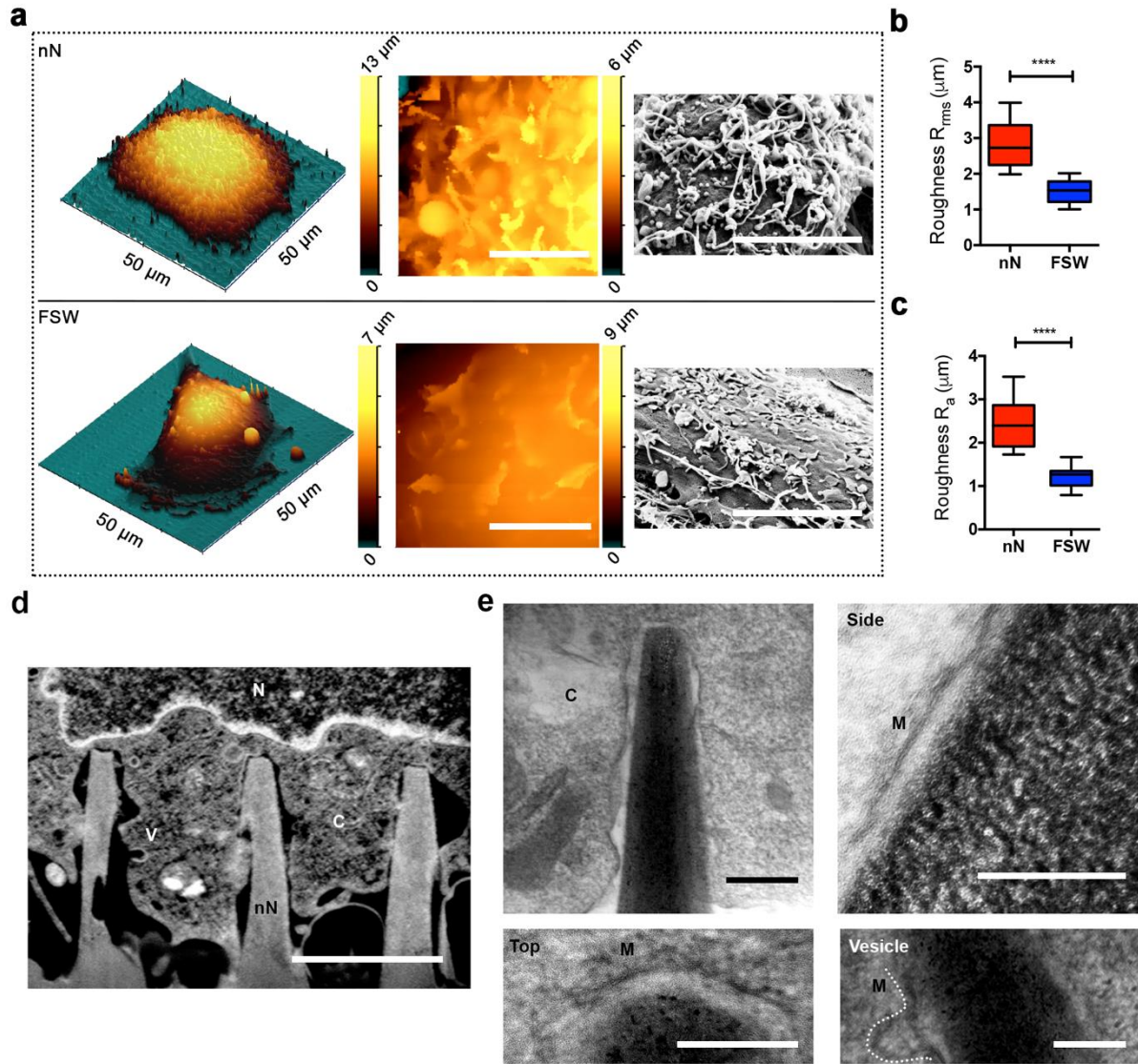[44] X. Xie, A. M. Xu, S. Leal-Ortiz, Y. Cao, C. C. Garner, N. A. Melosh, *ACS Nano* **2013**, *7*, 4351.

Figure 1. Cell membrane response to nanoneedle (nN) interfacing. (a) Nanoneedle interfacing induces membrane ruffling. 3D SICM image of a hMSC cultured on nanoneedles (top) or flat silicon wafer (FSW, bottom) for 6 hours (left). A zoomed-in 2D SICM scan (10 μm x 10 μm) (middle) and SEM image of the apical membrane (right). Scale bars = 5 μm. (b-c) Nanoneedle interfacing increases membrane roughness. Surface roughness R_{rms} (b) and Ra (c) of apical membrane of hMSCs on nanoneedles compared to FSW measured by SICM. Box plot shows center line as median, first and third quartile data range, and whiskers to minimum and maximum. ****$p < 0.0001$ (two-tailed unpaired Student's t-test), n = 8 cells for nN and n = 11 cells for FSW. (d-e) Cell membrane integrity is observed at the nanoneedle interface. C = cytosol, V = vesicle, N = nucleus, M = membrane. (d) Representative FIB-SEM image of an orthogonal cross-section of an hMSC on nanoneedles after 6 hours of interfacing. Scale bar = 2 μm. (e) TEM of FIB lift-out thin sections of the hMSC-nanoneedle interface. Clockwise: overview of a representative nanoneedle; nanoneedle side; vesicle located at the side of a nanoneedle; nanoneedle top. Scale bar = 200 nm.
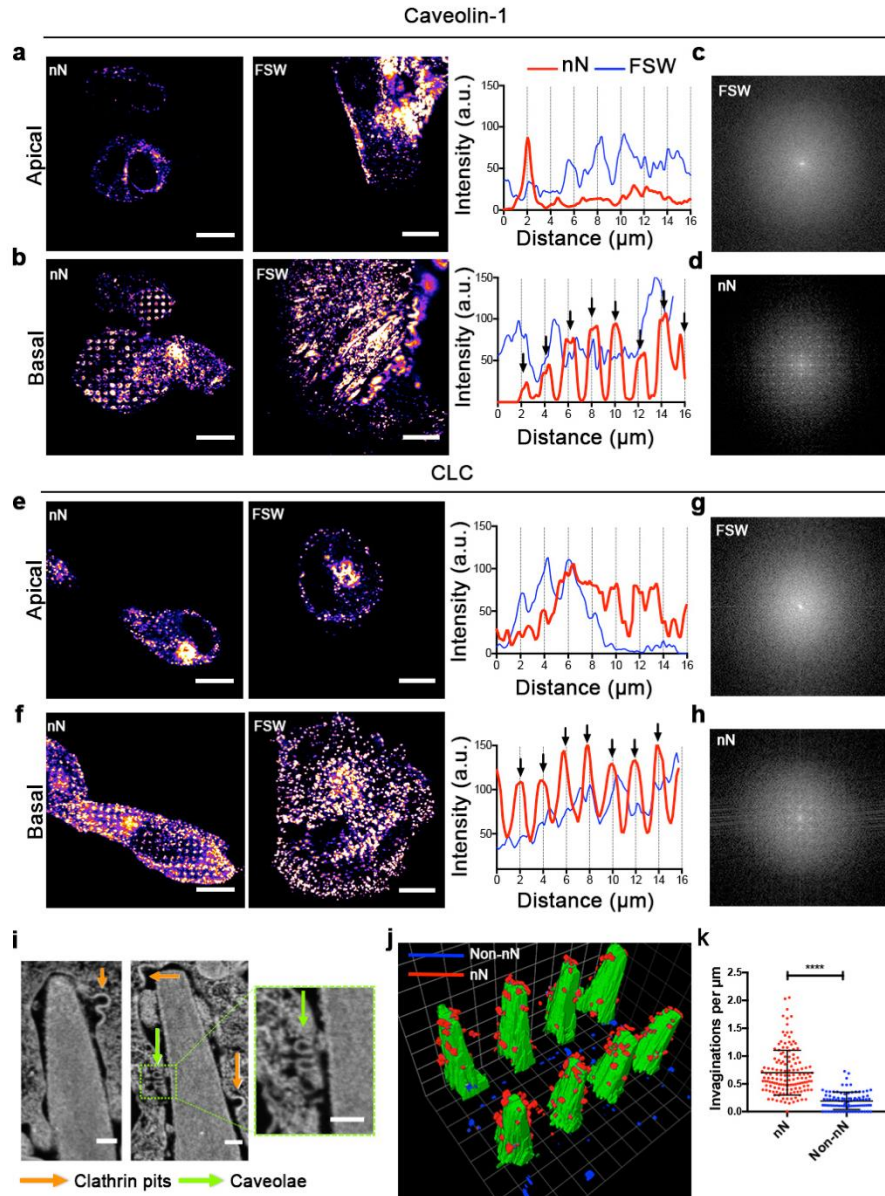
13

Figure 2. Nanoneedles locally activate endocytosis. (a-d) Caveolin-1 (Cav-1) accumulates around nanoneedles. (a-b) Confocal fluorescence images of caveolin-1 after 6 hours in the (a) apical and (b) basal membrane of hMSCs cultured on nanoneedles or FSW and their respective line intensity profiles over the cells. Arrows in line intensity plots indicate 2 μm intervals matching the distance between individual nanoneedles. (c-d) Upon interfacing, Cav-1 at the basal membrane acquires the same periodicity as the nanoneedles as assessed by Fourier transform analysis of the basal surface of hMSCs in panels a and b. (e-f) Clathrin accumulates around nanoneedles. Confocal fluorescence images of clathrin light chain (CLC) after 6 hours in the (e) apical and (f) basal membrane of hMSCs cultured on nanoneedles or FSW and their respective intensity profiles along the dashed lines. (g-h) Upon interfacing, clathrin at the basal membrane acquires the same periodicity as nanoneedles as assessed by Fourier transform analysis of the basal surface of hMSCs in panels e and f. Scale bars = 10 μm. (i-k) Endocytic vesicles accumulate around nanoneedles. (i) FIB-SEM image interface showing two classes of endocytic vesicles accumulating around nanoneedles: clathrin pits (orange arrows) and caveolae (green arrows). Scale bars = 100 nm. j) 3D reconstruction of the cell-nanoneedle interface over two consecutive rows of nanoneedles highlighting vesicular structures present in the membrane at nanoneedle (red) and non-nanoneedle (blue) locations. (k) Quantification of vesicular invaginations in the membrane from FIB-SEM data at nanoneedle and non-nanoneedle locations. Plot shows mean ± S.D., N = 4, n = 11 (cells), ****$p < 0.0001$ (two-tailed unpaired Student's t-test).
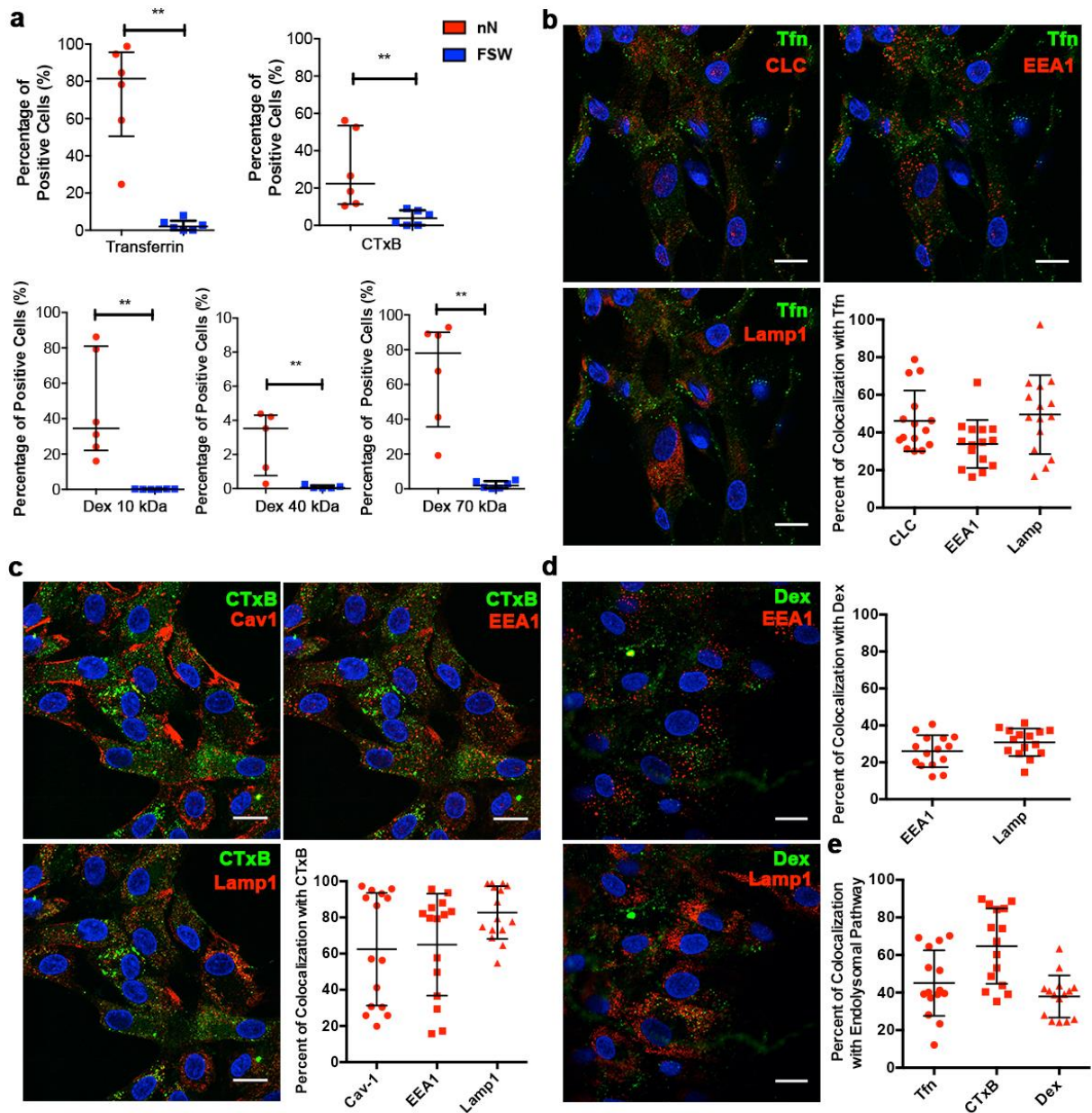
Figure 3. Nanoinjection enhances the uptake of pathway-specific cargo, which localizes within the endolysosomal system**. (a)** Nanoinjection enhances uptake of Transferrin (Tfn), Cholera toxin B subunit (CTxB) and Dextrans (Dex) of different sizes. Flow cytometry analysis showing the percentage of positive cells successfully internalizing pathway specific payloads by nanoinjection or FSW delivery at 24 hours. Clockwise – Tfn, a clathrin mediated endocytosis cargo, CTxB, a caveolae-specific cargo, and Dex 10 kDa, 40 kDa, 70 kDa, micropinocytosis specific cargo. Data presented as median with interquartile range. N = 3, n = 2 **p = 0.0022 for Tfn, CTxB, Dex 10 kDa, Dex 70 kDa and **p = 0.0079 for Dex 40 kDa (Mann-Whitney test). **(b)** Transferrin fate. Representative confocal images of a plane above the nanoneedles and quantification of Tfn (green) co-localization with CLC (clathrin light chain), EEA1 (early endosome antigen 1) and LAMP1 (lysosome-associated membrane protein 1) at 24 hours. **(c)** Cholera Toxin fate. Representative confocal images of a plane above the nanoneedles and quantification of CTxB co-localization with Cav-1, EEA1 and LAMP1 at 24 hours. d) Dextran fate. Representative confocal images of a plane above the nanoneedles and quantification of Dex 10 kDa co-localization with EEA1 and LAMP1 at 24 hours. Quantified data represented scatter dot plots with bars representing mean ± S.D., N = 1, n = 3 biological replicates, at least 5 images per n. Scale bars = 20 μm. **(e)** Quantification of Tfn, CTxB and Dex 10 kDa localization with their pathway-specific endocytosis carriers and trafficking components (Tfn with CLC, EEA1 and LAMP1, CTxB with Cav-1, EEA1 and LAMP1 and Dex10 with EEA1 and LAMP1). Quantified data presented as scatter dot plots with bars representing mean ± S.D., N = 1, n = 3 biological replicates, at least 5 images per n.
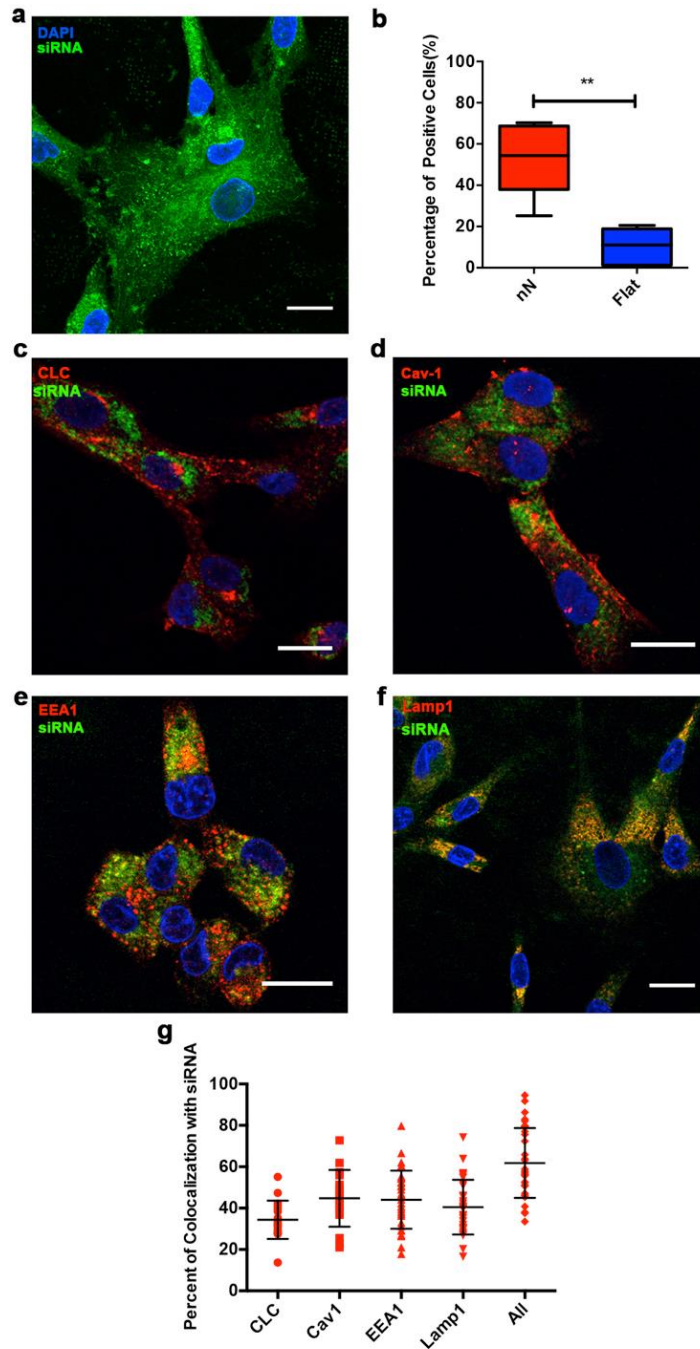
15

Figure 4. Nano-injected siRNA partly localizes across the endolysosomes while retaining cytosolic activity. (a-b) Nanoinjection enhances siRNA delivery. (a) Maximal Z-stack projection of hMSCs above the nanoneedles showing fluorescently labelled Cy3-siRNA-GAPDH (green) in the cell after 24 hours of interfacing. (b) Flow cytometry data of Cy3-siRNA uptake in hMSCs mediated by nanoneedles compared to FSW after 24 hours. Box plot shows center line as median, first and third quartile data range, and whiskers to minimum and maximum. **$p = 0.0022$ (Mann-Whitney test), N = 4, n = 2. (c-f) Representative confocal images of Cy3-siRNA co-localization with (c) CLC, (d) Cav-1, (e) EEA1, and (f) LAMP1. Scale bars = 20 μm. (g) Co-localization of endocytic carrier proteins (CLC, Cav-1), endosomes (EEA1) and late endosomes/lysosomes (LAMP1) and their combination (All) with Cy3-siRNA. Values reported as aligned scatter plot of percentages of Cy3-siRNA pixels overlapping with indicated components of the endolysosomal system (Mander's coefficient). Lines represent mean ± S.D.   N = 3, n = 2 for LAMP1, EEA1, N = 3, n = 1 for CLC, Cav-1. 5-10 images per sample.

16

Table of Contents

Nanoneedles have recently emerged as a safe and effective tool for intracellular delivery of therapeutic cargo. However, the mechanisms by which nanoneedles provide intracellular access are yet to be elucidated. This study investigates how porous silicon nanoneedle arrays interface with the cell membrane to facilitate intracellular delivery of various biological cargo.

Keywords: nanoneedles, biointerface, porous silicon, drug delivery, endocytosis

Sahana Gopal, Ciro Chiappini*, Jelle Penders, Vincent Leonardo, Hyejeong Seong, Stephen Rothery, Yuri Korchev, Andrew Shevchuk*, Molly M. Stevens*

Title Porous silicon nanoneedles modulate endocytosis to deliver biological payloads

ToC figure
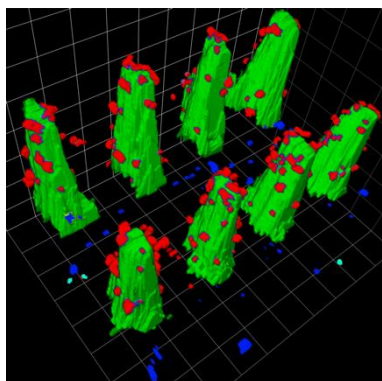
Supporting Information

Title Porous silicon nanoneedles modulate endocytosis to deliver biological payloads

Author(s), and Corresponding Author(s)*
Sahana Gopal[1,2], Ciro Chiappini[3], Jelle Penders[2], Vincent Leonardo[2], Hyejeong Seong[2] Stephen Rothery[4], Yuri Korchev[1], Andrew Shevchuk[1], Molly M. Stevens[2,5]*

Experimental Section

Antibodies and reagents

Anti-Caveolin-1 was purchased from Abcam (ab2910), Anti-clathrin light chain was purchased from Novus Biologicals (NBP2-14913), Anti-EEA1 (C45B10), Anti-LAMP1 (D4O1S) were purchased from Cell Signaling Technologies. Anti-Cy3-PE was purchased from Santa Cruz Biotechnologies. Transferrin-Alexa488, Cholera Toxin B subunit-Alexa488, Albumin-AlexaFluor®488, Dextran-TexasRed (10kDa, 40kDa and 70kDa) and GAPDH siRNA-Cy3 were purchased from ThermoFisher Scientific.

Nanoneedle fabrication and surface treatment

Nanoneedles were fabricated according to our established protocols.[1] We deposited a layer (120 nm) of low stress silicon nitride over p-type (0.01-0.02 Ω cm) Si wafer (100 mm). We patterned clear field dots (0.6 μm) with 2 μm pitch using contact UV photolithography uniformly through the wafer using NR9-250P photoresist (Futurrex, USA) in an MA6 mask aligner (K. Suss, Germany). The pattern was transferred into the silicon nitride layer by reactive ion etching in CF_4 gas. Electroless deposition of $AgNO_3$ salt (0.02 M) in a aqueous solution of HF (10%) for 2 minutes generated dendritic Ag nanoparticles selectively on the exposed silicon. Metal assisted chemical etching in H_2O_2 (1%), HF (10%) aqueous solution for 8.5 minutes generated porous silicon pillars underneath the silver nitride dots with interspersed porous silicon grass. The grass was removed, and the pillars shaped into cones by reactive ion etching in SF_6 gas. The wafer was diced in 8 x 8 mm dies for further use. Nanoneedle and flat silicon wafer (FSW) substrates were treated with oxygen plasma for 10-20 minutes (PlasmaPrep II,

18

Gala Instrumente, Germany). Nanoneedle and FSW substrates were treated with oxygen plasma for 10-20 minutes (PlasmaPrep II, Gala Instrumente, Germany).

Cell culture

Human mesenchymal stem cells (hMSC) were purchased from Lonza and cultured in MSCGM-CD (Lonza) or MSC Basal Media (MSCBM) (Lonza) with supplementation according to the manufacturer's instructions. When ~80% confluent, hMSCs were detached with trypsin-EDTA (0.05%, v/v, Invitrogen) and seeded onto FSW or nanoneedles substrates placed in a 24 well plate in Minimum Essential Media alpha (Gibco) with hMSC-graded foetal bovine serum (10%, v/v, Gibco) and Penicillin/Streptomycin (1%, v/v, Gibco). HMSCs were cultured on FSW and nanoneedle substrates at either passage 4 or passage 5 and seeded at a density of 20,000 cells per square cm unless otherwise specified.

Scanning ion conductance microscopy

SICM images of live hMSC cells were acquired in hopping probe scanning mode using a home-built microscope described previously.[2] Pipettes of approximately 100 nm were pulled from borosilicate glass (O.D. = 1 mm, I.D. = 0.5 mm, Intracel, Cambridge, UK) using a P-2000 laser puller (Sutter Instruments). Ion current measurements were conducted using Axopatch 200B amplifiers (Molecular Devices). Pipettes were filled with sterile filtered PBS for each experiment. For imaging, a bias potential of 200 mV was used. Ion current traces were tracked using pClamp10 (Molecular Devices). Cells cultured on nanoneedles and FSW for 6 hours were fixed in methanol-free paraformaldehyde solution (PFA, 4%, v/v, EM Sciences) for 15 minutes, washed with PBS and placed in 35 mm dishes in PBS. The pipette was immersed, current detected and approached over the sample using a set point of 0.3-0.4% drop in current. Cells were located by observing the z-retraction of the piezo when an area was scanned in x and y directions. A quick low-resolution scan was conducted to confirm the presence of the cell. The area containing the cell was selected and scanned at high resolution. Due to the high aspect ratio of the nanoneedle substrate, a pre-scan hop size of 10 μm was used when imaging cells on

nanoneedles. Images were analyzed using a home-written SICM Image viewer and surface roughness values were obtained using free, open source Gwyddion software for scanning probe microscopy data visualization and analysis (www.gwyddion.net).

Scanning electron microscopy

hMSCs cultured on nanoneedles or FSW were fixed in glutaraldehyde (GA, 2.5%, v/v, EM Sciences) for 30 minutes at room temperature. Samples were treated with OsO_4 (1%, v/v, EM Sciences) for 1 hour in sodium cacodylate buffer (0.1 M). Samples were washed twice in double distilled water for 5 minutes and dehydrated with a series of graded ethanol concentrations (20, 30, 50, 70, 80, 90%) and finally in 100% ethanol 4 times for 5 minutes each. Samples were treated with hexamethyldisilazane (Sigma) for 5 minutes and air dried after which they were mounted on aluminium stubs using carbon tape and sputter-coated with chromium (10 nm, Quorum 150T). Samples were visualized using a Zeiss Sigma300 SEM at an accelerating voltage of 5 kV and a working distance of 5 mm and secondary ion detector.

FIB-SEM sample preparation

hMSCs cultured on nanoneedles or FSW were fixed with GA, treated with OsO_4 and washed as above. Samples were treated with tannic acid (1%, v/v, Sigma) in water for 1 hour and washed with water. Samples were stained with uranyl acetate solution (1%, v/v, EM Sciences) for a minimum of 2.5 hours in the dark and proceeded to dehydration in ethanol as mentioned above. Resin embedding was conducted with epoxy resin embedding kit (Epon812, Sigma) at 3:1, 2:1, 1:1, 1:2 (v/v) of ethanol to resin for 2.5-3 hours each. Pure resin was infiltrated the following day for 3 hours, twice. Excess resin was washed off with ethanol twice, with air drying the sample between washes. Samples were left to polymerize for 48 hours at 60° C.

FIB-SEM imaging and analysis

Samples were sputtered with chromium (10 nm) or gold (20 nm) and imaged using Auriga CrossBeam Workstation (Zeiss). Cells on nanoneedles were located using the SEM and the stage was tilted to 54° and a tilt correction of 36° was applied. The same cell was located using

20

the FIB beam at a working distance of 5 mm. For 3D reconstructions, an imaging interval yielding sections of 30 nm was used by milling with 1 nA:30 kV milling current. For vesicle number analysis, the sample was milled at 1 nA:30 kV until a row of nanoneedles appeared and a single image obtained at the estimated tallest part of the nanoneedles-membrane interface. Non-nanoneedles locations were also imaged in the same cell as a control. SEM images were obtained with an accelerating voltage of 1.6 kV using a backscattered electron detector.

For 3D reconstruction, sequential images were aligned manually using Fiji and Amira (FEI). Images were manually segmented and reconstructed for nanoneedle, cell membrane and vesicle at nanoneedle locations and non-nanoneedle locations. For quantification of vesicle numbers, the length of the basal membrane in each image was calculated using the Fiji plug-in Simple Neurite Tracer. The number of vesicles in each image at nanoneedle and non-nanoneedle locations were counted manually with the point tool in Fiji.

Lift-out and TEM

Lamellae of hMSCs seeded on nanoneedles were prepared for TEM/STEM imaging by FIB-SEM lift-out using a Helios Nanolab 600 (FEI) equipped with a Ga^+ ion beam and a micromanipulator (Omniprobe, Oxford Instruments plc, Oxfordshire, United Kingdom). SEM imaging was performed at 2 kV and 0.17 nA and FIB milling at 30 kV with currents ranging from 28 pA to 2.8 nA, FIB polishing was performed down to 5 kV and 8 pA. A cell of interest was located by SEM imaging, showing normal morphology and proper preservation (Figure S3a). The sample was oriented to have the nanoneedle rows perpendicular to the FIB direction. First a rough trench was milled in the front of the cell at 2.8 nA, then the region of interest was approached by milling at 0.92 nA while simultaneously imaging in SEM mode. After ensuring the cell staining and ultrastructure preservation was adequate, milling was continued until the start of the row of nanoneedles included in the region of interest (Figure S3b). Platinum was deposited on top (1-1.5 μm wide) by Ga^+ assisted GIS at 93 pA − 0.28 nA, up to a thickness of 1-2 μm. Further trenches were milled behind the region of interest and on the sides, freeing the

lamella except for attachment to the base (Figure S3c). The lamella was approached with the micromanipulator needle and attached by platinum deposition. The base of the lamella was milled loose and for structural stability of the lamella up to 4 micron of silicon substrate was included in the lift-out (Figure S3d). The middle post of a 3-post copper lift-out grid (Omniprobe, EM Sciences) was approached with the micromanipulator and the lamella was attached to the post by further platinum deposition, after which the micromanipulator was cut loose (Figure S3e). The lamella was thinned to electron transparency, 100-120 nm, by FIB milling equally on both front and back of the lamella ensuring the apex of the nanoneedles is in the centre of the lamella (pre-thinning Figure S3f, post-thinning Figure S3g side view, Figure S3h front view).

Immunofluoresence staining, imaging and analysis

hMSCs on nanoneedles and FSW were fixed with PFA (4%, v/v) for 15 minutes in PBS. Samples were washed in PBS and treated with Triton X-100 (0.25%, v/v, Sigma) for 5 minutes. Samples were washed with PBS and incubated with normal serum (5%, v/v, ThermoFisher Scientific) of the same species as the secondary antibody for 1 hour at room temperature. Primary antibodies to caveolin-1 (1:300), clathrin light chain (1:300), EEA1 (1:200) and LAMP1 (1:200) were allowed to incubate overnight at 4° C in BSA (0.1%, w/v) in PBS. For LAMP1 staining, PFA fixed samples were treated with methanol for 10 minutes at -20° C. For double immunofluorescence staining with multiple primary antibodies of the same species, primary antibodies to caveolin-1 and clathrin light chain were applied as mentioned and samples were washed in PBS. Samples were blocked using goat anti-rabbit Fab' fragment (Jackson Immunolabs). Secondary fluorescent anti-goat antibodies were applied to detect caveolin-1 and clathrin. Following this, antibodies to EEA1 and LAMP1 were applied to these samples for detection with secondary fluorescent antibodies (Control experiment – Supplementary Figure 6).

Samples were washed 3 times for 5 minutes in PBS and secondary antibodies were applied for 1 hour at room temperature in the dark. Samples were washed extensively in PBS, flipped upside down into chamber slides (Ibidi) containing Vectashield (Vector Labs) for imaging by confocal microscopy. Images were obtained using a Leica SP5 inverted microscope using a 63X oil immersion objective.

For colocalization analysis, multi-channel images of 16-bit and 1024 x 786 pixel resolution were imported into Volocity Software (6.3, Perkin-Elmer) using automatic thresholding using the Costes' method. This approach finds the best linear regression of the two channels of interest intensities over all the pixels, and then the thresholds are moved along the regression line until Pearson's correlation for pixels below threshold is less than or equal to 0. In this way, all intensity values below the threshold (i.e. cytosolic) were excluded from the analysis. Mander's coefficient of overlap was selected and converted to a percentage for statistical analysis. For endolysomal pathway colocalization analysis, multi-channel images were overlaid in a single channel and analyzed for colocalization with delivered payload as mentioned above.

Nanoneedle-mediated biomolecule delivery

Fluorescently labelled Transferrin (25 μg ml^{-1}), Albumin (40 μg ml^{-1}), Cholera Toxin (5 μg ml^{-1}), Dextrans (1 mg ml^{-1}, 10 kDa, 40 kDa and 70 kDa) and GAPDH-siRNA (1 μM) were each reconstituted in a buffer containing glycine (0.25 M) and KCl (400 mM), pH adjusted to 5.0. Nanoneedle and FSW chips were plasma and UV treated prior to loading cargo. For siRNA delivery, chips were pre-treated with HCl (2 M) for 10 minutes after plasma and UV treatment followed by rinsing in distilled water and air drying. 10 μl of each solution was adsorbed for 45 minutes in a humidified chamber in the dark. Chips were washed once with the buffer and air-dried. Chips loaded with siRNA were washed further with Buffer RPE (Qiagen) and air-dried. Cells were cultured on loaded substrates for 24 hours after which they were fixed in PFA (4%, v/v) or assessed for uptake by flow cytometry. For siRNA experiments, hMSCs were thawed from frozen, cultured to 70% confluence and seeded at P4.

For assessing the uptake from cargo-loaded nanoneedles and FSW substrates, hMSCs were dry seeded by applying a cell suspension (50 µl) containing 80-100,000 cells that stayed only on the chip and did not flood the well plate. After 2 hours, after the cells had attached to the substrates, the media was gently topped up to an optimum volume. This ensured that all cells seeded remained on the substrates and did not attach to the bottom of the wells.

Flow cytometry

Media was aspirated and chips were transferred to a new well plate and washed with PBS. Cells were detached from substrates with trypsin and centrifuged at 300g for 7 minutes at 4°C. Cells were resuspended in PBS and centrifuged once again, after which they were resuspended in Cell Staining Buffer (200 µl, BioLegend). Samples were measured with a BD LSRFORTESSA (BD) cell analyzer equipped with 488 nm and 561 nm lasers and 530/30 582/15 and 610/20 filters. Raw data were analyzed with FlowJo and equal population gates were applied in order to allow direct comparison between experimental groups.

Quantitative real time polymerase chain reaction (qRT-PCR)

Cells on nanoneedle and FSW substrates were treated with Trizol reagent (Life Technologies), mixed with chloroform (1:5, Chloroform:Trizol) and separated by centrifugation for 15 minutes at 4°C at 12,000g. RNA was isolated from the aqueous phase after the centrifugation using Direct-zol RNA MiniPrep Kit (Zymo Research) based on the manufacturer's instructions. cDNA was synthesized using High Capacity cDNA Reverse Transcription Kits (Applied Bioscience) according to the manufacturer's instructions. qRT-PCR was performed with the PowerUP SYBR Green Master Mix (Applied Biosystems), with cDNA (2.5 ng) and forward and reverse primers (500 nM), using a StepOne Plus machine (Applied Biosystems). The StepOne Plus protocol ran as 95°C for 2 minutes followed by 40 cycles of denaturation at 95°C for 3 seconds and annealing at a temperature 60°C for 30 seconds. Cycles-to-threshold (Ct) values were automatically obtained from the StepOne software v2.3. These values were

exported to the Excel file and manually processed to generate fold change expression values. The expression of each gene of interest was normalized to the geometric mean of the expression of at least two housekeeping genes PPIA and RPL13A, generating the $\Delta C(t)$ value, and expression of $2^{-\Delta C(t)}$ relative to the control.

Protein Extraction and Western Blotting

Media was gently aspirated and nanoneedle and FSW substrates were transferred to a new well plate on ice. Samples were rinsed two times with ice cold PBS. Cell lysate was extracted and pooled from 8 substrates for each sample in 300 µl of cell lysate extraction buffer that consisted of Urea (4 M, Ultrapure, Sigma-Aldrich), NaCl (150 mM, Sigma-Aldrich), PhosSTOP (Roche), and complete EDTA free protease inhibitor cocktail (Roche) by scraping within the well plate on ice. An immersion probe was used to sonicate lysates by applying a pulse (10 seconds, 200 W). Lysates were centrifuged at 15,000xg for 10 minutes at 4°C and supernatant was extracted. Qubit protein assay (Q33211, Thermo) was used to quantify protein extracted using fluorometric quantitation instrument Qubit 4 Fluorometer (Thermo). Lysates were prepared for Sodium Dodecyl Sulphate Polyacrylamide Gel Electrophoresis (SDS-PAGE) with 4x sample buffer containing β-mercaptoethanol in a 3:1 ratio and heated at 80°C for 5 minutes. Protein samples were separated on a gel by SDS-PAGE in TGS running buffer (Bio-rad) for 45 minutes at 100 V. The gel was transferred to a blot using Transblot-turbo (Bio-rad). Blots were probed with Cav-1 (1:1000), CLC (1:1000) and respective secondary antibodies (Li-Cor IR 680, IR 800, 1:1000) prepared in iBind solution (SLF1019, ThermoFisher Scientific) for fluorescent antibodies according the manufacturer's instructions. Immunoblotting was conducted using iBind Flex western device (ThermoFisher Scientific) according to the manufacturer's instructions. Blots were imaged using a Li-Cor Odyssey imaging system.
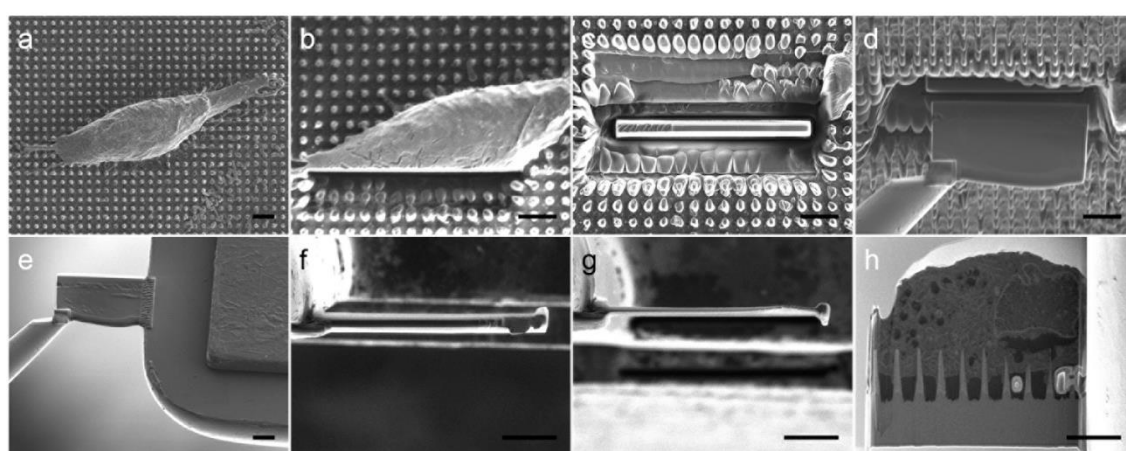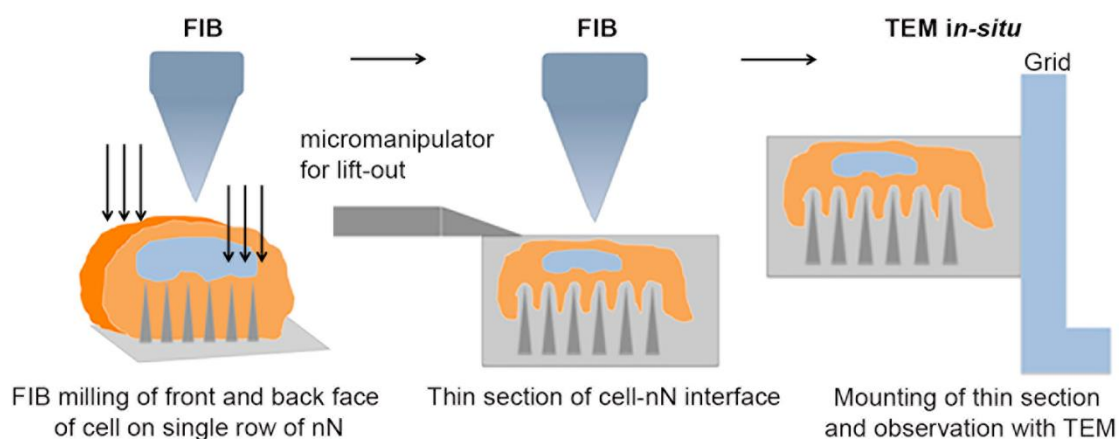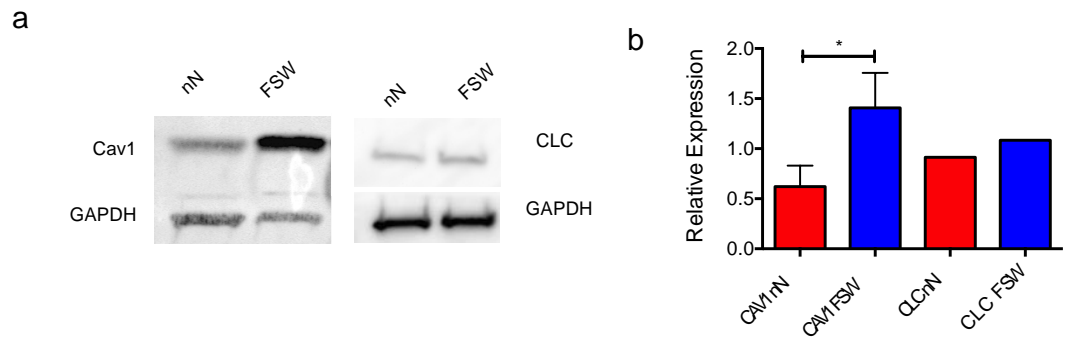
Supplementary Figures
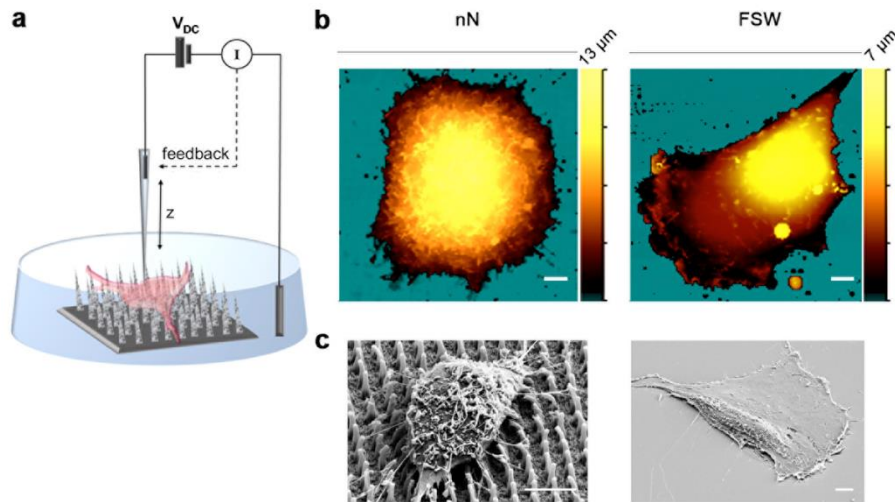
Supplementary Figure 1 a) Schematic of hopping mode SICM for scanning cells on nanoneedles. In hopping mode SICM as used in this setup the probe approaches the sample from above thereby preventing the risk of collision particularly with high aspect ratio nanostructures such as our nanoneedles. Fixed samples are placed in a 35 mm dish in PBS. Voltage is applied between the electrodes in the pipette probe and in the bath producing an ion current. At every pixel, the pipette approaches the sample until a drop in current (I) of 0.25-1 % is achieved. At this point the height (z) is recorded and stored in a topographical map. The pipette is then retracted and moved to the next imaging location. b) 2D topographical maps of hMSCs on nanoneedles and FSW after 6 hours of culture. c) SEM images of hMSCs cultured on nanoneedles and FSW for 6 hours showing membrane ruffling. Scale bars = 5 μm.
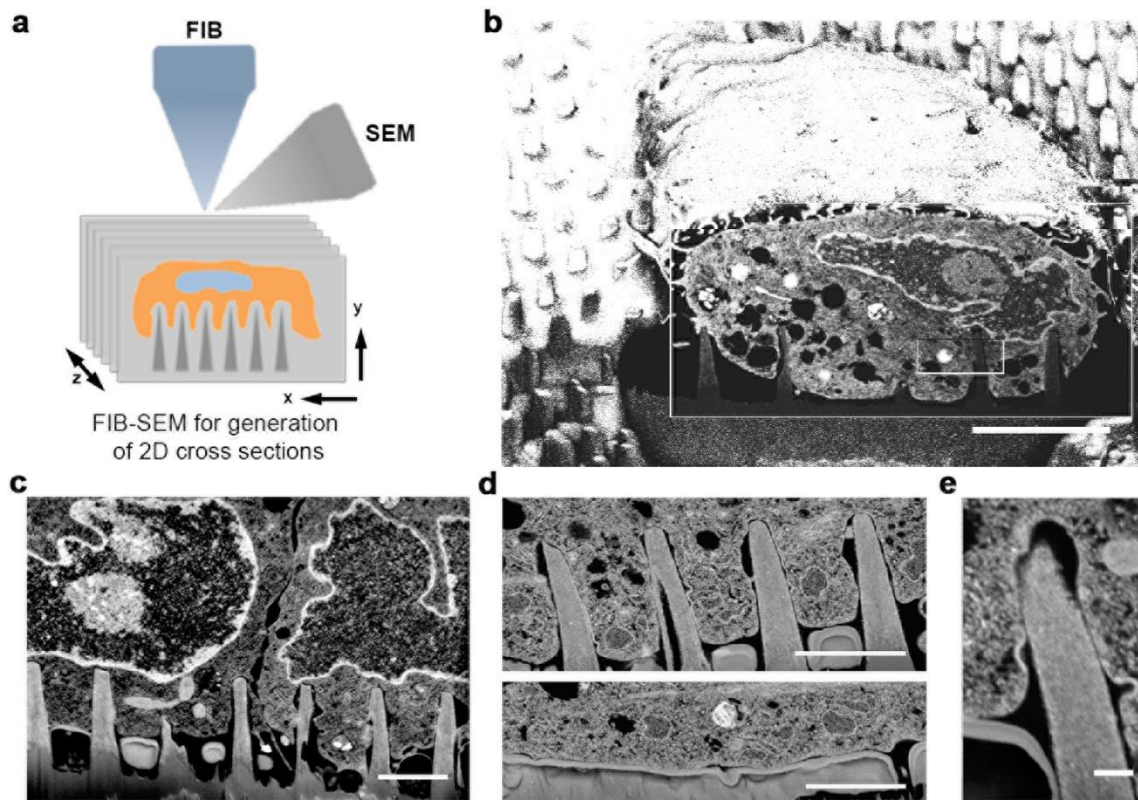
Supplementary Figure 2 a) Schematic of the FIB-SEM set up. 2D cross-sections of the cell-nanoneedle interface. 2D cross-sections of the cell-nanoneedle interface milled by the focused ion (gallium) beam at 30 nm intervals. Samples are milled orthogonally and the newly milled face is imaged using an SEM backscattered electron detector at the coincidence point (where the beams meet). b) Zoomed-out SEM image of the cross-section of an hMSC cultured on nanoneedles after 6 hours. Scale bar = 6 μm c) SEM images of a milled cross-section indicating two cells in contact while interfacing with nanoneedles. Scale bar = 2 μm. d) SEM images of milled cross sections of nanoneedle (top) and non-nanoneedle (bottom) regions indicating intact membranes. Scale bar = 2 μm. e) Zoomed-in view of the membrane-nanoneedle interface indicating membrane-wrapping and clathrin-like vesicles. Scale bar = 200 nm.

Supplementary Figure 3 Schematic and images of process flow for FIB lift out for generation of thin-sections. The sample (a) is milled at the front (b) and back (c) to generate a section of the cell with a single row of nanoneedles underneath it. d) A micro-manipulator is attached to the section using platinum deposition and the sample is milled below the base of the nanoneedles. e) The lift out section is mounted on a grid and the micromanipulator is released (f), after which the sample is thinned further (g) to desired thickness. h) the final front face of the thin section containing regions of interest prior to TEM imaging. Scale bars = 5 µm.

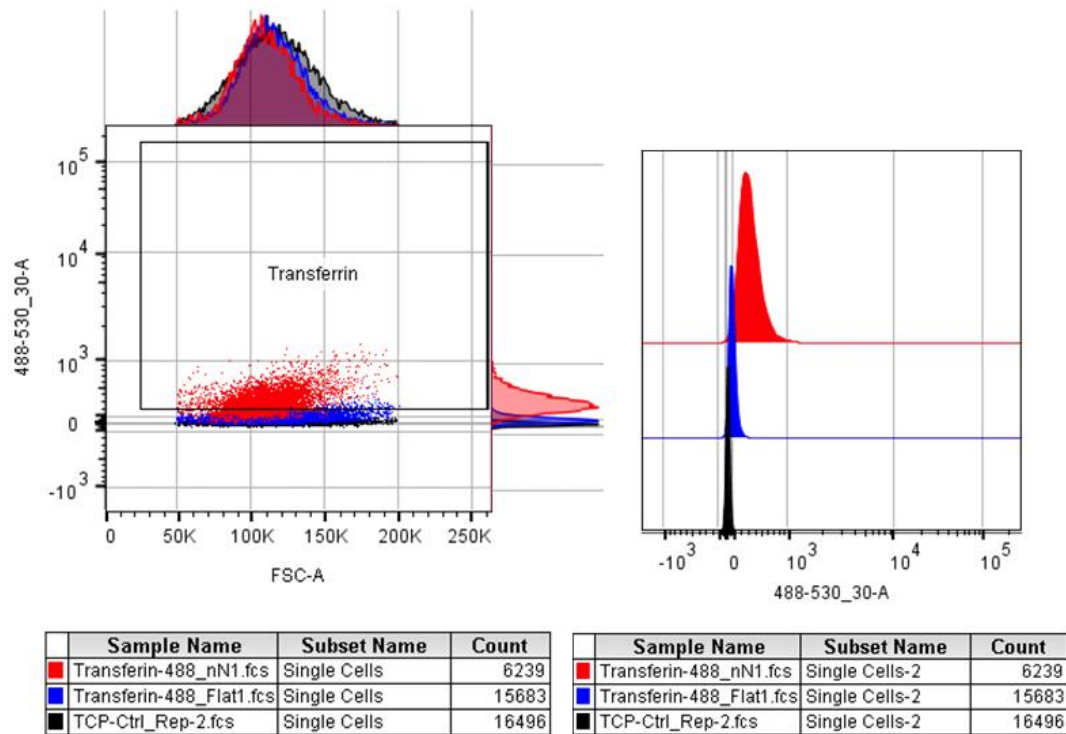**Supplementary Figure 4** a) Western blot of CAV-1, CLC and GAPDH in hMSCs after 6 hours of interfacing with nN or FSW. b) Quantification of western blot of CAV-1 and CLC normalized to GAPDH. N = 4 (CAV-1), N =1 (CLC), n = 8 (pooled chips). Data presented as mean ± S.D., $p*$ = 0.0286, two-tailed Mann-Whitney non-parametric test.
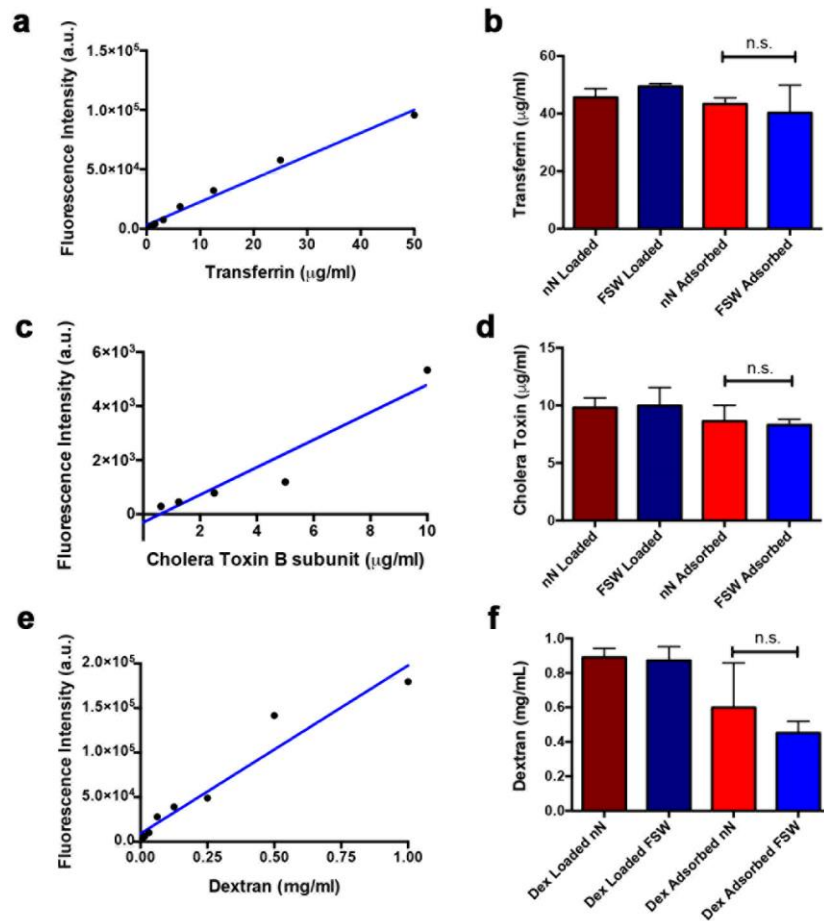
Supplementary Figure 5 a) Standard curve of Transferrin b) Quantities of Transferrin initially loaded on nanoneedle and FSW, and finally adsorbed on nanoneedle and FSW after 45 minutes of incubation. c) Standard curve of Cholera Toxin B subunit d) Quantities of Cholera Toxin B subunit initially loaded on nanoneedle and FSW, and finally adsorbed on nanoneedle and FSW after 45 minutes of incubation. e) Standard curve of Dextran 10 kDa. f) Quantities of Dextran 10 kDa initially loaded on nanoneedle and FSW, and finally adsorbed on nanoneedle and FSW after 45 minutes of incubation. Data shown as mean ± S.D., n = 3, n.s.= not significant (two-tailed Mann-Whitney test).
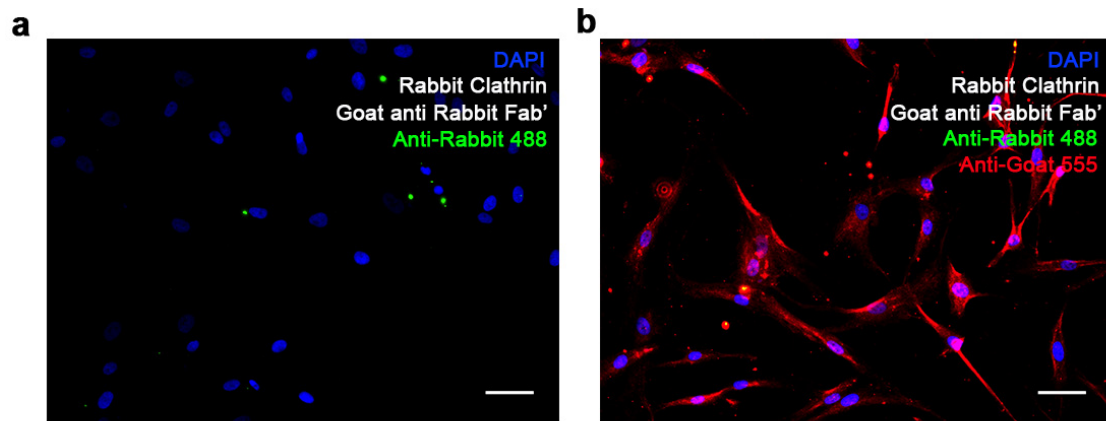
Supplementary Figure 6 a) Fluorescence microscopy images of hMSCs immunolabeled with rabbit anti-clathrin antibody, incubated with goat-anti rabbit Fab' fragment followed by donkey anti-rabbit secondary AlexaFluor®488 and anti-rabbit secondary AlexaFluor®488 and b) the same with the addition anti-goat AlexaFluor® 555. Images indicate that primary rabbit immuno-label is converted to goat by goat anti-rabbit Fab' fragment. Scale bars = 20 μm.

Sample Name	Subset Name	Count
Transferin-488_nN1.fcs	Single Cells	6239
Transferin-488_Flat1.fcs	Single Cells	15683
TCP-Ctrl_Rep-2.fcs	Single Cells	16496

Sample Name	Subset Name	Count
Transferin-488_nN1.fcs	Single Cells-2	6239
Transferin-488_Flat1.fcs	Single Cells-2	15683
TCP-Ctrl_Rep-2.fcs	Single Cells-2	16496

Supplementary Figure 7 Flow cytometry scatter plots and mean fluorescence intensity for clathrin-specific cargo Transferrin AlexaFluor®488 for hMSCs on cultured on nanoneedles (red), FSW (blue) and control TCP (no cargo, black) after 24 hours.

Sample Name	Subset Name	Count
Cholera-Toxin-488_nN2.fcs	Single Cells	16083
Cholera-Toxin-488_Flat1.fcs	Single Cells	16068
TCP-Ctrl_Rep-1.fcs	Single Cells	16538

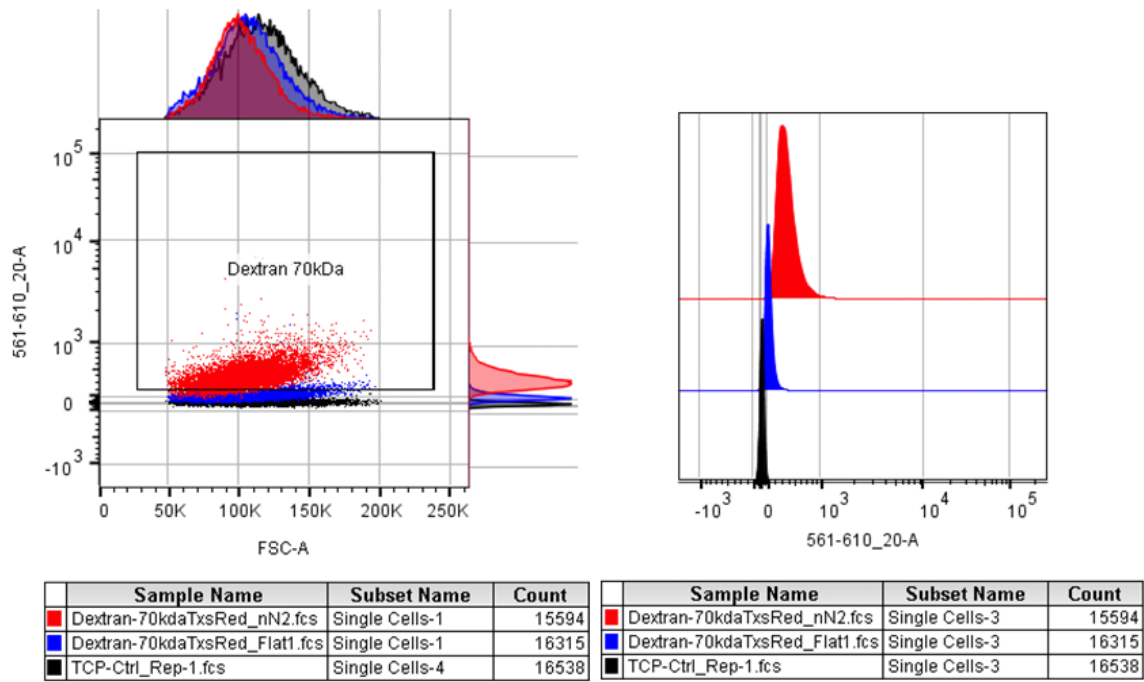| Sample Name	Subset Name	Freq. of Total
Cholera-Toxin-488_nN2.fcs	Single Cells-2	80.4
Cholera-Toxin-488_Flat1.fcs	Single Cells-2	80.3
TCP-Ctrl_Rep-1.fcs	Single Cells-2	82.7
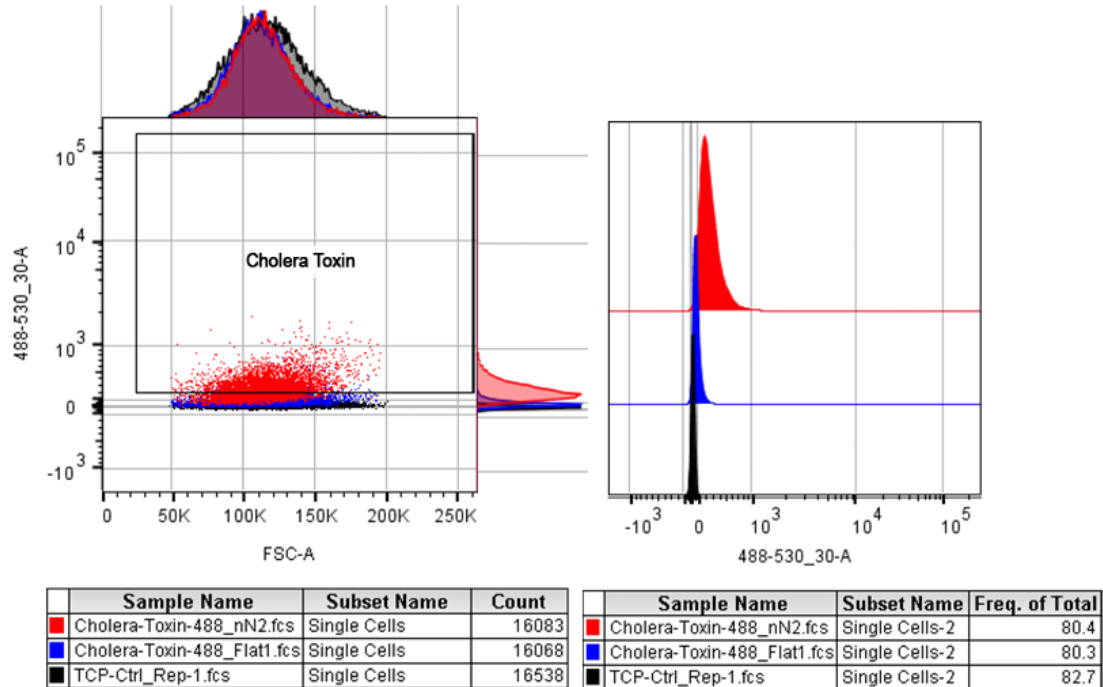
Supplementary Figure 8 Flow cytometry scatter plots and mean fluorescence intensity for caveolae-specific cargo Cholera toxin AlexaFluor®488 for hMSCs on cultured on nanoneedles (red), FSW (blue) and control TCP (no cargo, black) after 24 hours.

32
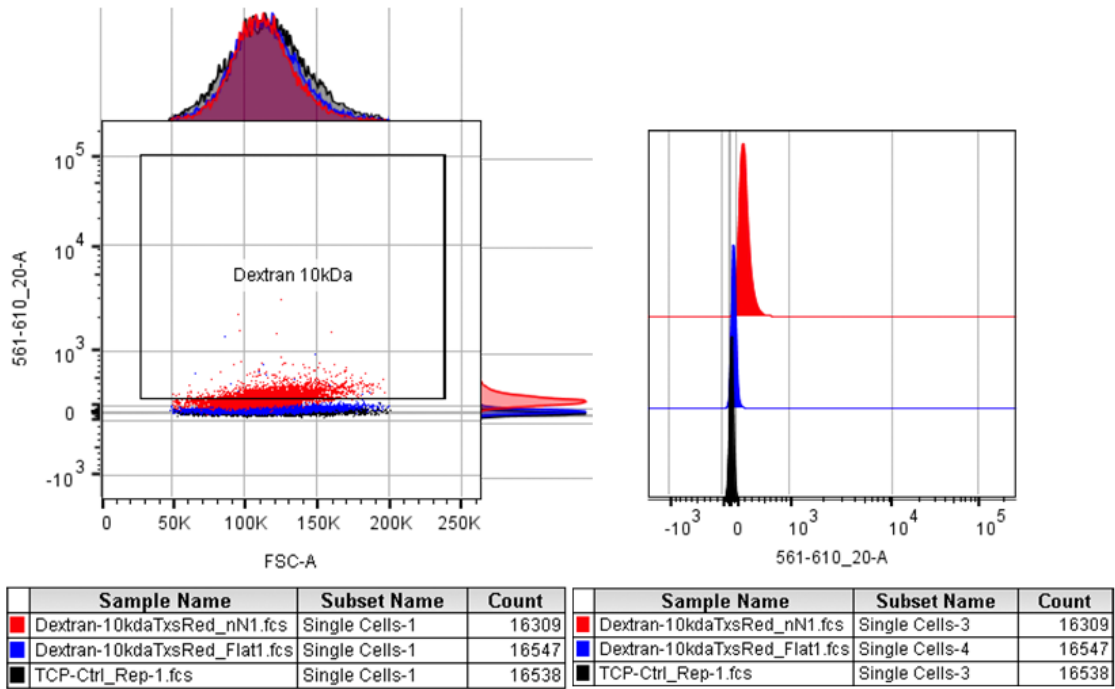
Supplementary Figure 9 Flow cytometry scatter plots and mean fluorescence intensity for micropinocytosis-specific cargo Dextran 10 kDa – TexasRed for hMSCs on cultured on nanoneedles (red), FSW (blue) and control TCP (no cargo, black) after 24 hours.
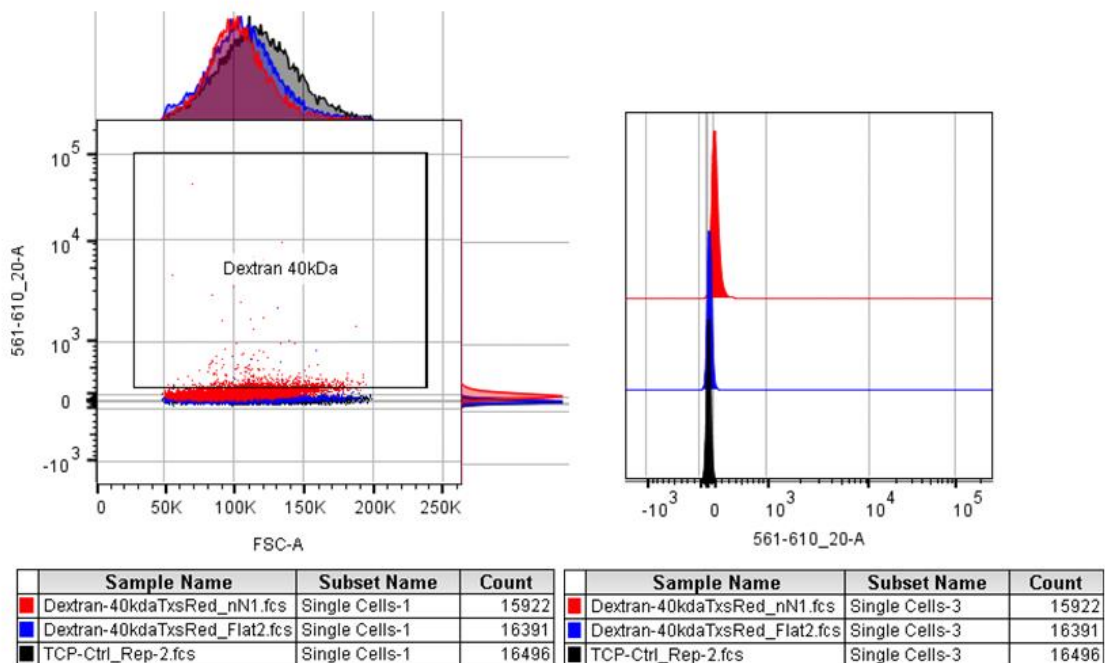
Supplementary Figure 10 Flow cytometry scatter plots and mean fluorescence intensity for micropinocytosis-specific cargo Dextran 40 kDa – TexasRed for hMSCs on cultured on nanoneedles (red), FSW (blue) and control TCP (no cargo, black) after 24 hours.

	Sample Name	Subset Name	Count
🟥	Dextran-70kdaTxsRed_nN2.fcs	Single Cells-1	15594
🟦	Dextran-70kdaTxsRed_Flat1.fcs	Single Cells-1	16315
⬛	TCP-Ctrl_Rep-1.fcs	Single Cells-4	16538

	Sample Name	Subset Name	Count
🟥	Dextran-70kdaTxsRed_nN2.fcs	Single Cells-3	15594
🟦	Dextran-70kdaTxsRed_Flat1.fcs	Single Cells-3	16315
⬛	TCP-Ctrl_Rep-1.fcs	Single Cells-3	16538

Supplementary Figure 11 Flow cytometry scatter plots and mean fluorescence intensity for micropinocytosis-specific cargo Dextran 70 kDa – TexasRed for hMSCs on cultured on nanoneedles (red), FSW (blue) and control TCP (no cargo, black) after 24 hours.

Experiment	GAPDH expression		Difference between control and siRNA (nN control – nN siRNA)	% Decrease (Difference/nN control *100)
	nN without siRNA delivery (control)	nN with siRNA delivery		
1	0.72	0.29	0.41	59.47%
2	0.84	0.57	0.68	32.19%
3	1.44	0.89	0.62	37.90%
		Mean	**0.57**	**43.19%**
		S.D.	**0.14**	**14.38%**

Table S1. Calculation of percentage decrease in expression of GAPDH per experimental replicate after nanoneedle-mediated delivery of GAPDH-siRNA. The difference between expression of GAPDH in control and siRNA treated samples in each experiment was used to calculate the percent change in expression compared to control. An average reduction in expression of 43% was achieved by siRNA-delivery via nanoneedle arrays.

Gene Name	Accession Number	Forward primer (5'-3') Reverse primer (3'-5')	Amplicon (bp)	Total primer concentration
GAPDH	NM_002046.4	GCACCGTCAAGGCTGAGAAC TGGTGAAGACGCCAGTGGA	138	500 nM
PPIA	NM_021130	CTTCACACGCCATAATGGC GTGATCTTCTTGCTGGTCTTG	273	500 nM
RPL13A	NM_012423	AAGTACCAGGCAGTGACAG CCTGTTTCCGTAGCCTCATG	100	500 nM

Table S2. qRT-PCR Primer Sequences

References

[1]   C. Chiappini, E. De Rosa, J. O. Martinez, X. Liu, J. Steele, M. M. Stevens, E. Tasciotti, *Nat Mater* **2015**, *14*, 532.
[2]   P. Novak, C. Li, A. I. Shevchuk, R. Stepanyan, M. Caldwell, S. Hughes, T. G. Smart, J. Gorelik, V. P. Ostanin, M. J. Lab, G. W. J. Moss, G. I. Frolenkov, D. Klenerman, Y. E. Korchev, *Nat Meth* **2009**, *6*, 279.